

Chaotic advection in a steady three-dimensional MHD flow

Julien Fontchastagner,^{1,*} Jean-François Scheid,^{2,†} Jean-Régis Angilella,^{3,‡} and Jean-Pierre Brancher^{2,§}

¹*Université de Lorraine, GREEN, Nancy 54000, France*

²*Université de Lorraine, CNRS, Inria, IECL, Nancy 54000, France*

³*Normandie Université, UNICAEN, UNIROUEN, ABTE, Caen 14000, France*

(Dated: May 31, 2024)

(**Preprint version**)

We investigate a real 3D stationary flow characterized by chaotic advection generated by a magnetic field created by permanent magnets acting on a weakly conductive fluid subjected to a weak constant current. The model under consideration involves the Stokes equations for viscous incompressible fluid at low Reynolds number in which the density forces correspond to the Lorentz force generated by the magnetic field of the magnets and the electric current through the fluid. An innovative numerical approach based on a mixed finite element method has been developed and implemented for computing the flow velocity fields with the electromagnetic force. This ensures highly accurate numerical results, allowing a detailed analysis of the chaotic behavior of fluid trajectories through the computations of associated Poincaré sections and Lyapunov exponents. Subsequently, an examination of mixing efficiency is conducted, employing computations of contamination and homogeneity rates, as well as mixing time. The obtained results underscore the relevance of the modeling and computational tools employed, as well as the design of the magnetohydrodynamic device used.

I. INTRODUCTION AND MOTIVATION

Mixing devices for highly viscous fluids or small Reynolds number flows have been studied during these last fifty years. The flow must exhibit chaotic streamlines which can be obtained by an efficient stretching and folding mechanism. Many classical mixing systems are used with turbulent flows producing random motions of particles. These devices are not very convenient for highly viscous flows because the energy to be supplied is too strong or because degradation of the product to be mixed can occur [1].

Chaotic advection has been studied in a general way [2, 3] and for two dimensional time dependent flows like flows between eccentric cylinders or flows induced by moving walls in a cavity [4, 5]. In three dimensions, the flows do not need to be time dependent to produce chaotic advection [6]: for instance, in open flows in a pipe with electrically conducting fluids submitted to high frequency magnetic fields [7, 8] or in the theoretical periodic flow studied in the PHD Thesis of V. Toussaint [9, 10]. In this paper, we consider a real steady flow in a box, similar to the textbook case of the previous Thesis consisting in the superposition of two stationary vortices and an orthogonal stationary vortex.

So we consider a viscous fluid weakly electrically conductive (slightly salted water for instance) filling a cube and crossed by a uniform horizontal current of density \mathbf{j}_0 and subjected to a magnetic field induced by a set of magnets. At first, if we study a simple situation where a constant vertical electric field \mathbf{h}_1 is imposed on a half volume and set to zero in the other part, as depicted in FIG. 1 (a), we can see that the liquid does not remain at rest and a swirl will appear [11].

The magnetic force ($\mathbf{f} = \mu_0 \mathbf{j}_0 \times \mathbf{h}$, where μ_0 is the magnetic permeability of the vacuum) is an horizontal and uniform vector field \mathbf{f}_1 in the part under the field and zero in the other part. The curl of this force is given by its tangential jump on the discontinuity surface Σ , $\mathbf{curl} \mathbf{f} = \mathbf{f}_1 \times \mathbf{n} \delta_\Sigma$ where δ_Σ is the Dirac distribution on Σ . As $\mathbf{curl} \mathbf{f}$ is not zero, the fluid cannot stay at rest. We also note that if \mathbf{j}_0 is rotated of an angle of $\frac{\pi}{2}$, \mathbf{f}_1 becomes parallel to \mathbf{n} and we get $\mathbf{curl} \mathbf{f} = \mathbf{0}$, so although the pressure is changed, the fluid remains at rest.

When $\mathbf{f} = \mathbf{f}_2$ in the middle and set to zero in the others sides, a pair of counter rotating vortices takes place, as we can see in FIG. 1 (b). These two forces \mathbf{f}_1 and \mathbf{f}_2 can be superimposed to generate two vortices with an orthogonal vortex in the fluid, thus defining a simple magnetohydrodynamic (MHD) mixing device which comprises only static sources. This situation is very close to the study made in [9] and [10] where chaotic advection is investigated from explicit formulae for the velocity field. In this article, the magnetic forces will no longer be chosen piecewise constant but they are numerically computed from Maxwell's equations. The velocity field in the fluid will then be computed with these magnetic forces using a vorticity – stream-function formulation of the Stokes equations.

* julien.fontchastagner@univ-lorraine.fr

† jean-francois.scheid@univ-lorraine.fr

‡ jean-regis.angilella@unicaen.fr

§ jean-pierre.brancher@univ-lorraine.fr

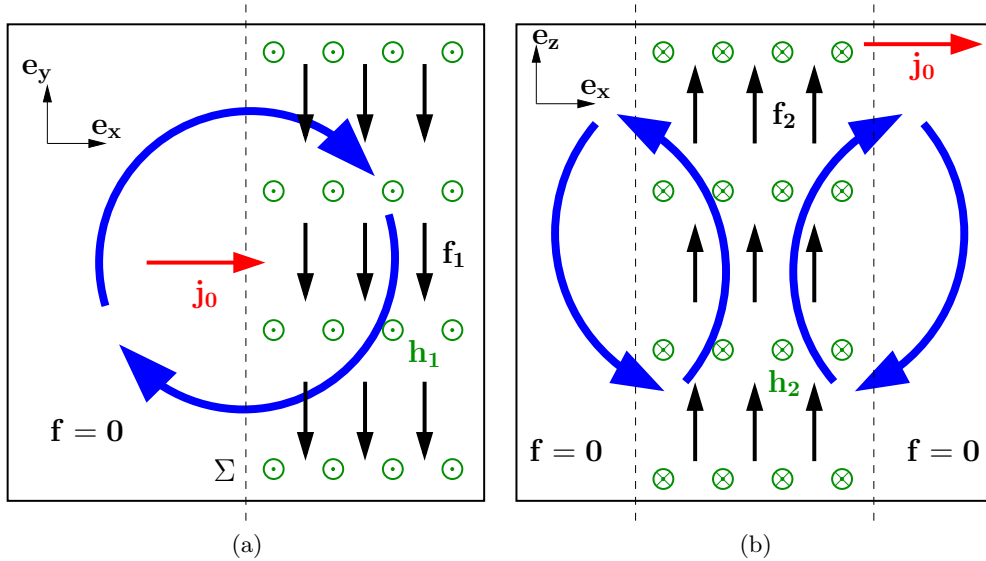


FIG. 1. Schematics of the considered fields: (a) First configuration creating one swirl in the (x, y) plane, and (b) Second configuration involving two vortices in the (x, z) plane.

In the next chapter, we give the equations of the coupled system we study for the magnetic fields with the Stokes flow. Then, numerical simulations will be performed for different parameters of the device magnetic field customization. The magnetic force that will be imposed to the fluid is a weighted average of the two forces \mathbf{f}_1 , \mathbf{f}_2 and the ratio of the two will be the customizing parameter of the device. We will show that chaotic advection can be obtained for specific choices of this ratio. The computation of Poincaré sections and Lyapunov exponents, among others, will provide a qualitative and quantitative study of the chaotic streamlines we obtain. In the final section, we will carry out a brief study of the mixing efficiency.

II. DESCRIPTION AND MODELLING OF THE MIXING MHD DEVICE

A. Principle and assumptions

A cubic tank of side length a containing a viscous fluid is considered. An uniform current density \mathbf{j}_0 (directed along the base vector \mathbf{e}_x) is imposed inside by a constant voltage drop. To generate the two vortex configurations described in the previous section, two pairs of magnets will be placed on each opposite side of the tank in two orthogonal directions as shown in FIG. 2. The first one (magnetised along \mathbf{e}_z and in red color in FIG. 2) is used to create a force similar to \mathbf{f}_1 as in Section I; and the second one (magnetised along \mathbf{e}_y and in blue color in FIG. 2)) should produce a force similar to \mathbf{f}_2 . The length and the depth of the magnets are equal to a whereas their width is equal to $\frac{a}{2}$.

The fluid in the tank is considered as incompressible Newtonian with a viscosity ν sufficiently high to be in a small Reynolds number case ($Re \ll 1$). The value of the current density is chosen to be sufficiently low compared to the magnetization of the permanent magnets so that its impact on the total magnetic field, and therefore on the total corresponding force, can be neglected [12]. The effect of gravity on the flow is also assumed to be negligible.

B. Non-dimensional governing equations

According to the previous assumptions, the studied flow in the tank (Ω_t domain) corresponds to a Stokes flow governing by the Stokes equations:

$$\begin{cases} \nu \Delta \mathbf{v} - \mathbf{grad} p + \mathbf{f} = \mathbf{0} \\ \text{div} \mathbf{v} = 0 \end{cases}, \text{ in } \Omega_t \quad (1)$$

with ν the dynamic viscosity of the fluid, \mathbf{v} its velocity, p the pressure, and \mathbf{f} the applied force density. No slip and impermeability conditions are imposed on the tank boundary Γ_t for the velocity field:

$$\mathbf{v} = \mathbf{0} \text{ on } \Gamma_t = \partial\Omega_t \quad (2)$$

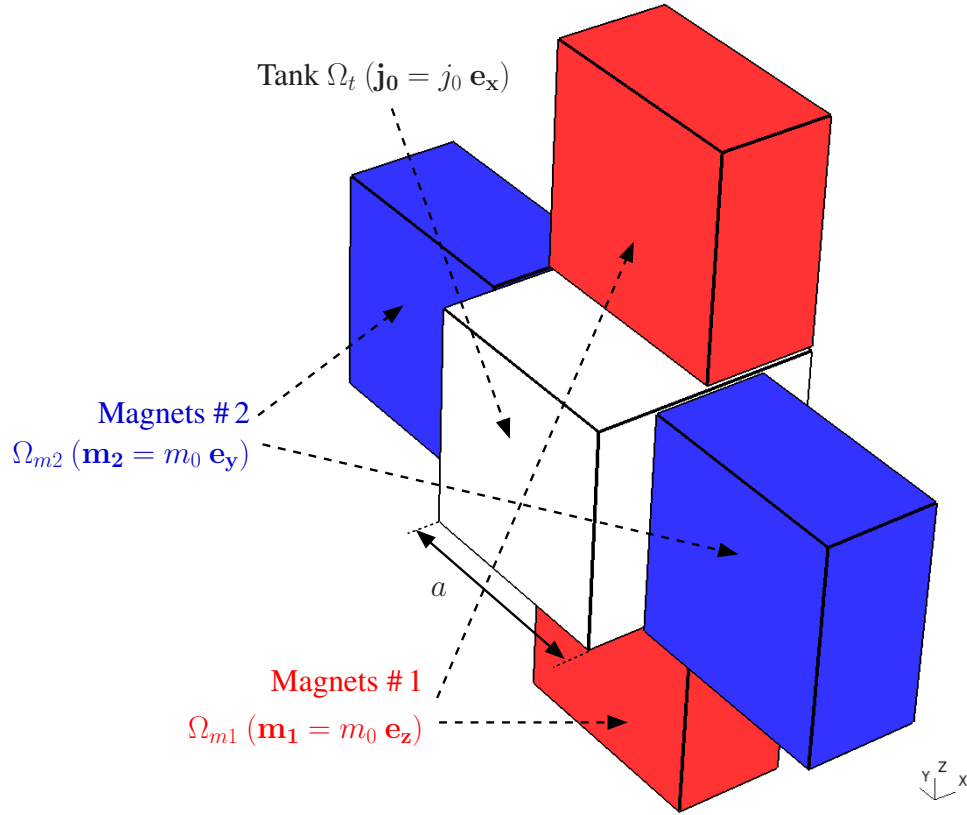


FIG. 2. Setup of the mixing MHD device

The applied force density in the tank corresponds to the Lorentz force and the contribution of each pair of magnets can be treated separately according to the superposition principle:

$$\mathbf{f} = \mu_0 \mathbf{j}_0 \times \mathbf{h} = \underbrace{\mu_0 \mathbf{j}_0 \times \mathbf{h}_1}_{\mathbf{f}_1} + \underbrace{\mu_0 \mathbf{j}_0 \times \mathbf{h}_2}_{\mathbf{f}_2} \quad (3)$$

where \mathbf{h}_i , $i = \{1, 2\}$ is the field produced by magnets $\#i$. In this way, due to the linearity of the Stokes equations, the velocity field \mathbf{v} in (1) can be decomposed in

$$\mathbf{v} = \mathbf{v}_1 + \mathbf{v}_2 \quad (4)$$

where each part \mathbf{v}_1 and \mathbf{v}_2 satisfies separately:

$$\begin{cases} \nu \Delta \mathbf{v}_i - \mathbf{grad} p_i + \mu_0 \mathbf{j}_0 \times \mathbf{h}_i = \mathbf{0} & \text{in } \Omega_t \\ \text{div } \mathbf{v}_i = 0 & \text{in } \Omega_t \\ \mathbf{v}_i = \mathbf{0} & \text{on } \Gamma_t = \partial\Omega_t \end{cases}, \text{ for } i = \{1, 2\} \quad (5)$$

The magnetic field and flux density in the overall domain Ω are governed by the Maxwell-Ampère and Maxwell-Thomson equations:

$$\mathbf{curl} \mathbf{h}_i = \mathbf{0}, \quad \text{div } \mathbf{b}_i = 0, \quad (6)$$

and both fields vanish far from the magnets ($\|\mathbf{x}\| \rightarrow \infty$). The source term at the origin of the magnetic flux density is due to the magnetization of the magnets, $\mathbf{m}_1 = m_1 \mathbf{e}_z$ for the magnets $\#1$ and $\mathbf{m}_2 = m_2 \mathbf{e}_x$ for the magnets $\#2$ (see FIG. 2). The magnetic behaviour law linking the flux densities \mathbf{b}_i and the magnetic fields \mathbf{h}_i is then

$$\begin{cases} \mathbf{b}_i = \mu_0 (\mathbf{h}_i + \mathbf{m}_i) & \text{in } \Omega_{mi} \\ \mathbf{b}_i = \mu_0 \mathbf{h}_i & \text{elsewhere} \end{cases}, \text{ for } i = \{1, 2\} \quad (7)$$

Extending magnet magnetizations as piecewise functions on the complete domain:

$$\mathbf{m}_i = \begin{cases} \mathbf{m}_i & \text{in } \Omega_{mi} \\ \mathbf{0} & \text{in } \Omega \setminus \Omega_{mi} \end{cases}, \quad (8)$$

the magnetic fields \mathbf{h}_1 and \mathbf{h}_2 are finally governed by

$$\begin{cases} \mathbf{curl} \mathbf{h}_i = \mathbf{0} & \text{in } \Omega \\ \mathbf{div}(\mathbf{h}_i + \mathbf{m}_i) = 0 & \text{in } \Omega \\ \lim_{\|\mathbf{x}\| \rightarrow \infty} \mathbf{h}_i = \mathbf{0} \end{cases}, \text{ for } i = \{1, 2\} \quad (9)$$

The side length of the cubic tank a is chosen as the characteristic length of the problem, and the non-dimensional position vector $\widehat{\mathbf{x}}$ is then defined by: $\mathbf{x} = a\widehat{\mathbf{x}}$. The norm j_0 of the current density can be expressed from the total current I_0 flowing through the system so that the non-dimensional current density can be defined by

$$\widehat{\mathbf{j}}_0(\widehat{\mathbf{x}}) = \frac{\mathbf{j}_0(\mathbf{x})}{j_0} = \frac{a^2}{I_0} \mathbf{j}_0(\mathbf{x}) \quad (10)$$

In the same way, a non-dimensional magnetization vector $\widehat{\mathbf{m}}_i$, and the corresponding $\widehat{\mathbf{h}}_i$ field are introduced as follow:

$$\widehat{\mathbf{m}}_i(\widehat{\mathbf{x}}) = \frac{\beta}{m_0} \mathbf{m}_i(\mathbf{x}), \quad \widehat{\mathbf{h}}_i(\widehat{\mathbf{x}}) = \frac{\beta}{m_0} \mathbf{h}_i(\mathbf{x}), \quad \text{for } i = \{1, 2\} \quad (11)$$

where β is an arbitrary scaling factor designed to avoid too low values of magnetic fields (and therefore forces and velocities) when solving the problem. By replacing in (9), the non-dimensional magnetic systems to be solved becomes

$$\left(\widehat{S}_{m,i} \right) \begin{cases} \mathbf{curl} \widehat{\mathbf{h}}_i = \mathbf{0} & \text{in } \widehat{\Omega} \quad \left(\Omega = a\widehat{\Omega} \right) \\ \mathbf{div} \left(\widehat{\mathbf{h}}_i + \widehat{\mathbf{m}}_i \right) = 0 & \text{in } \widehat{\Omega} \\ \lim_{\|\widehat{\mathbf{x}}\| \rightarrow \infty} \widehat{\mathbf{h}}_i = \mathbf{0} \end{cases}, \text{ for } i = \{1, 2\} \quad (12)$$

Next, let us denote v_0 and p_0 the characteristic velocity and pressure of the fluid, and define the non-dimensional corresponding quantities:

$$\widehat{\mathbf{v}}_i(\widehat{\mathbf{x}}) = \frac{\mathbf{v}_i(\mathbf{x})}{v_0}, \quad \widehat{p}_i(\widehat{\mathbf{x}}) = \frac{p_i(\mathbf{x})}{p_0}, \quad \text{for } i = \{1, 2\} \quad (13)$$

The fluid equations becomes

$$\Delta \widehat{\mathbf{v}}_i - \frac{a p_0}{\nu v_0} \mathbf{grad} \widehat{p}_i + \frac{\mu_0 I_0 m_0}{\nu v_0 \beta} \widehat{\mathbf{j}}_0 \times \widehat{\mathbf{h}}_i = \mathbf{0}, \quad \text{for } i = \{1, 2\} \quad (14)$$

By choosing

$$v_0 = \frac{\mu_0 I_0 m_0}{\nu \beta} \quad \text{and} \quad p_0 = \frac{\mu_0 I_0 m_0}{\beta}, \quad (15)$$

the fluid system can be simplified as follows:

$$\left(\widehat{S}_{f,i} \right) \begin{cases} \Delta \widehat{\mathbf{v}}_i - \mathbf{grad} \widehat{p}_i + \widehat{\mathbf{j}}_0 \times \widehat{\mathbf{h}}_i = \mathbf{0} & \text{in } \widehat{\Omega}_t \quad \left(\Omega_t = a\widehat{\Omega}_t \right) \\ \mathbf{div} \widehat{\mathbf{v}}_i = 0 & \text{in } \widehat{\Omega}_t \\ \widehat{\mathbf{v}}_i = \mathbf{0} & \text{on } \widehat{\Gamma}_t = \partial\widehat{\Omega}_t \end{cases}, \text{ for } i = \{1, 2\} \quad (16)$$

Finally, by sequentially resolving $\left(\widehat{S}_{m,1} \right)$ and $\left(\widehat{S}_{m,2} \right)$, then $\left(\widehat{S}_{f,1} \right)$ and $\left(\widehat{S}_{f,2} \right)$, we obtain the two velocity fields $\widehat{\mathbf{v}}_1$ and $\widehat{\mathbf{v}}_2$. The real physical ones \mathbf{v}_1 and \mathbf{v}_2 can be simply deduced by multiplying by v_0 .

In the remainder of this article, we will be concerned only with non-dimensional quantities, and for convenience and the sake of clarity, these will be referred to without the hat ($\widehat{\cdot}$) symbol.

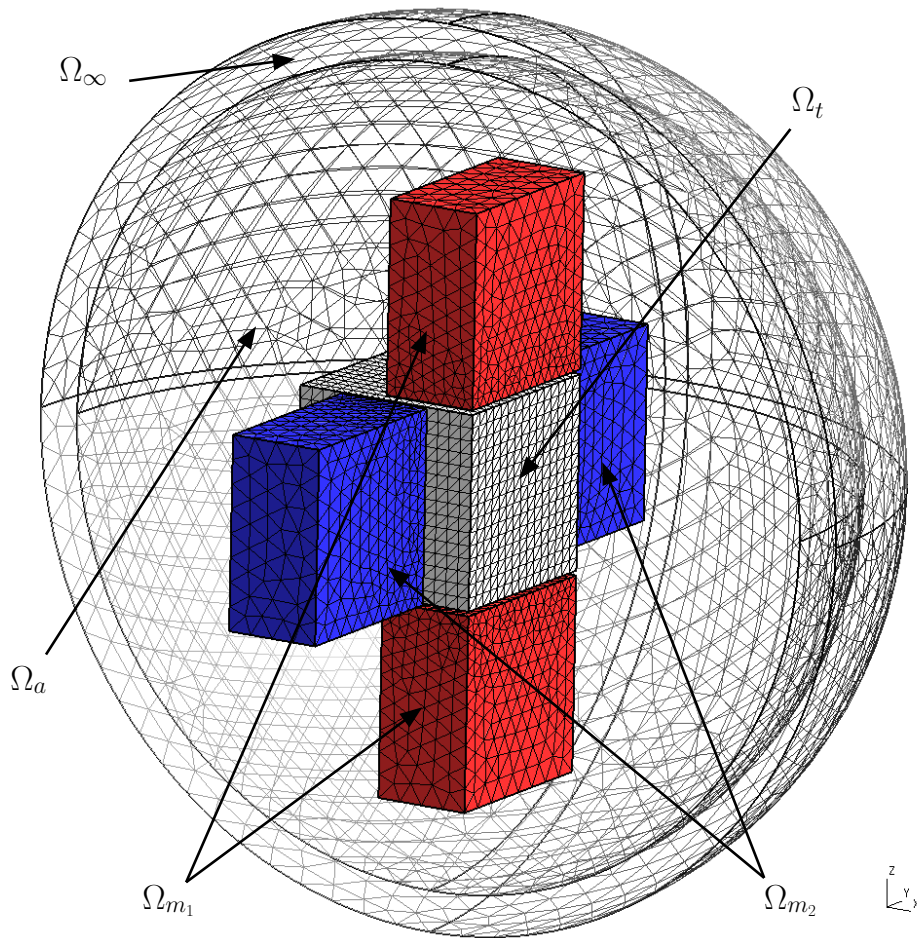


FIG. 3. Representation of the total computation domain, and the corresponding mesh used for the numerical computations (control parameter $ne = 15$)

III. NUMERICAL COMPUTATIONS OF FIELDS

The authors of the present paper wish to solve all the governing equations with the same computation tool, in order to avoid possible errors of projection or interpolation of results on different meshes or function spaces. Mixed finite elements methods based on both nodal and edge basis functions, provide an efficient and convenient framework for solving problems of low-frequency computational electromagnetism [13–15]. But they can also be used to correctly approximate the Stokes system [13, 16]. In what follows, we will describe how this type of mixed finite elements methods can be used to numerically solve the full set of equations with accuracy, in particular by developing a dedicated vorticity – stream-function formulation for the Stokes equations.

A. Magnetic fields: scalar magnetic potential formulation

The overall domain of computation $\Omega = \Omega_t \cup \Omega_{m_1} \cup \Omega_{m_2} \cup \Omega_a \cup \Omega_\infty$ is represented in FIG. 3. Ω_t corresponds to the tank, Ω_{m_1} and Ω_{m_2} to the pairs of magnets, and Ω_a the air region around them. Their union form the domain of interest $\Omega_i = \Omega_t \cup \Omega_{m_1} \cup \Omega_{m_2} \cup \Omega_a$ in which the magnetic fields are wanted. The external boundary of Ω_i is that of a sphere of radius R_i . This region is surrounded by a spherical finite shell Ω_∞ with inner and outer radii respectively R_i and R_o . This will be useful to deal with the open boundary condition on fields as explain below.

The spaces $L^2(\Omega)$ and $\mathbf{L}^2(\Omega)$ can be defined by:

$$L^2(\Omega) = \left\{ u : \int_{\Omega} u(\mathbf{x})^2 d\mathbf{x} < \infty \right\}, \quad \text{and} \quad \mathbf{L}^2(\Omega) = \left\{ \mathbf{u} : \int_{\Omega} \|\mathbf{u}(\mathbf{x})\|^2 d\mathbf{x} < \infty \right\} \quad (17)$$

They permit to define the Sobolev space $\mathbf{H}(\mathbf{grad}, \Omega)$, more commonly known as $\mathbf{H}^1(\Omega)$:

$$\begin{aligned} \mathbf{H}(\mathbf{grad}, \Omega) &= \{u \in \mathbf{L}^2(\Omega) : \mathbf{grad} u \in \mathbf{L}^2(\Omega)\} \\ &= \{u \in \mathbf{L}^2(\Omega) : \partial_x u, \partial_y u, \partial_z u \in \mathbf{L}^2(\Omega)\} = \mathbf{H}^1(\Omega) \end{aligned} \quad (18)$$

The Maxwell-Ampère equation $\mathbf{curl} \mathbf{h}_i = \mathbf{0}$ implies that there exists a magnetic scalar potential $\phi_i \in \mathbf{H}(\mathbf{grad}, \Omega)$ such that:

$$\mathbf{h}_i = -\mathbf{grad} \phi_i \quad (19)$$

To deal with the $\mathbf{h}_i \xrightarrow{\|\mathbf{x}\| \rightarrow \infty} \mathbf{0}$ condition, a bijective transformation that maps all the region $\mathbb{R}^3 \setminus \Omega_i$ onto Ω_∞ is constructed thanks to the relation:

$$\|\mathbf{x}\| = R_i \frac{R_o - R_i}{R_o - \|\mathbf{X}\|} \quad (20)$$

where \mathbf{X} is the position vector in the shell Ω_∞ [17]. The considered transformation $\mathcal{F} : \mathbb{R}^3 \setminus \Omega_i \rightarrow \Omega_\infty$ is therefore defined by:

$$\mathbf{X} = \mathcal{F}(\mathbf{x}) = \frac{\|\mathbf{X}\|}{\|\mathbf{x}\|} \mathbf{x} = \left[\frac{R_o}{\|\mathbf{x}\|} - \frac{R_i(R_o - R_i)}{\|\mathbf{x}\|^2} \right] \mathbf{x} \quad (21)$$

The open-boundary conditions on \mathbf{h}_1 and \mathbf{h}_2 can be replaced by imposing homogeneous Dirichlet conditions on ϕ_1 and ϕ_2 on $\Gamma_\infty = \partial\Omega$ (the sphere of radius R_o). We will also use the transformation \mathcal{F} and its jacobian matrix $\mathbf{J}_\mathcal{F}$ to bring back all integrals posed on $\mathbb{R}^3 \setminus \Omega_i$ to Ω_∞ .

The second equation of $(S_{m,i})$ becomes:

$$\mathbf{div}(\mathbf{grad} \phi_i - \mathbf{m}_i) = 0 \quad \text{in } \Omega \quad (22)$$

Multiplying (22) by a test function $\xi_i \in \mathbf{H}_0(\mathbf{grad}, \Omega) = \{u \in \mathbf{H}(\mathbf{grad}, \Omega) : u|_{\Gamma_\infty} = 0\}$, then using the transformation \mathcal{F} to write down the integrals terms over $\mathbb{R}^3 \setminus \Omega_i$ to Ω_∞ and finally integrating by parts, we obtain the weak form $(\Sigma_{m,i})$ of the system $(S_{m,i})$ given by (12):

$$(\Sigma_{m,i}) \left\{ \begin{array}{l} \text{Find } \phi_i \in \mathbf{H}_0(\mathbf{grad}, \Omega) \text{ such that: } \forall \xi_i \in \mathbf{H}_0(\mathbf{grad}, \Omega), \\ \int_{\Omega_i} \mathbf{grad} \phi_i \cdot \mathbf{grad} \xi_i \, d\mathbf{x} - \int_{\Omega_{m_i}} \mathbf{m}_i \cdot \mathbf{grad} \xi_i \, d\mathbf{x} \\ + \int_{\Omega_\infty} \mathbf{J}_\mathcal{F}^{-1} \mathbf{grad} \phi_i \cdot \mathbf{J}_\mathcal{F}^{-1} \mathbf{grad} \xi_i \, |\det \mathbf{J}_\mathcal{F}| \, d\mathbf{X} = 0 \end{array} \right. \quad (23)$$

Once ϕ_i is computed from (23), the force density involved in the non-dimensional Stokes flow systems in Ω_t will be:

$$\mathbf{f}_i = -\mathbf{j}_0 \times \mathbf{grad} \phi_i \quad (24)$$

B. Flows velocities: Vorticity – stream-function formulation

Let us begin by defining the spaces:

$$\mathbf{H}(\mathbf{curl}, \Omega_t) = \{\mathbf{u} \in \mathbf{L}^2(\Omega_t) : \mathbf{curl} \mathbf{u} \in \mathbf{L}^2(\Omega_t)\} \quad (25)$$

$$\mathbf{H}_0(\mathbf{curl}, \Omega_t) = \{\mathbf{u} \in \mathbf{H}(\mathbf{curl}, \Omega_t) : \mathbf{u} \times \mathbf{n}|_{\Gamma_t} = \mathbf{0}\} \quad (26)$$

where Γ_t is the boundary of Ω_t ($\Gamma_t = \partial\Omega_t$). It is possible to rewrite the Stokes system (16) in terms of the vorticity fields $\boldsymbol{\omega}_i \in \mathbf{H}(\mathbf{curl}, \Omega_t)$ defined by $\boldsymbol{\omega}_i = \mathbf{curl} \mathbf{v}_i$:

$$\mathbf{curl} \boldsymbol{\omega}_i + \mathbf{grad} p_i - \mathbf{f}_i = \mathbf{0} \quad (27)$$

And the fact that $\mathbf{v}_i = \mathbf{0}$ on Γ_t directly implies:

$$0 = \mathbf{curl} \mathbf{v}_i \cdot \mathbf{n} = \boldsymbol{\omega}_i \cdot \mathbf{n} \quad \text{on } \Gamma_t \quad (28)$$

Since \mathbf{v}_i is divergence free, there exists a vector potential called stream function $\boldsymbol{\psi}_i \in \mathbf{H}_0(\mathbf{curl}, \Omega_t)$ such that [18]:

$$\mathbf{v}_i = \mathbf{curl} \boldsymbol{\psi}_i, \quad \text{and} \quad \text{div} \boldsymbol{\psi}_i = 0 \quad (29)$$

Using it and applying the \mathbf{curl} operator to the first equation of the system $(S_{f,i})$, we obtain:

$$\begin{cases} \mathbf{curl} \mathbf{curl} \boldsymbol{\omega}_i = \mathbf{curl} \mathbf{f}_i, & \text{div} \boldsymbol{\omega}_i = 0 & \text{in } \Omega_t \\ \boldsymbol{\omega}_i = \mathbf{curl} \mathbf{curl} \boldsymbol{\psi}_i, & \text{div} \boldsymbol{\psi}_i = 0 & \text{in } \Omega_t \\ \boldsymbol{\omega}_i \cdot \mathbf{n} = 0, \quad \boldsymbol{\psi}_i \times \mathbf{n} = \mathbf{0}, \quad \mathbf{curl} \boldsymbol{\psi}_i \times \mathbf{n} = \mathbf{0} & \text{on } \Gamma_t \end{cases} \quad (30)$$

The vorticity $\boldsymbol{\omega}_i$ can be separated into $\boldsymbol{\omega}_i = \boldsymbol{\omega}_i^0 + \boldsymbol{\omega}_i^*$ where $\boldsymbol{\omega}_i^0 \in \mathbf{H}_0(\mathbf{curl}, \Omega_t)$ is a regular part and $\boldsymbol{\omega}_i^* \in \mathbf{H}(\mathbf{curl}, \Omega_t)$ is the harmonic contribution [19, 20]. We rewrite the global system in two weakly coupled subsystems as follows:

$$\left\{ \begin{array}{l} -\Delta \boldsymbol{\omega}_i^0 = \mathbf{curl} \mathbf{curl} \boldsymbol{\omega}_i^0 = \mathbf{curl} \mathbf{f}_i \\ \text{div} \boldsymbol{\omega}_i^0 = 0 \\ \boldsymbol{\omega}_i^0 \times \mathbf{n}|_{\Gamma_t} = \mathbf{0} \end{array} \right\}, \quad \left\{ \begin{array}{l} -\Delta \boldsymbol{\psi}_i = \mathbf{curl} \mathbf{curl} \boldsymbol{\psi}_i = \boldsymbol{\omega}_i^0 + \boldsymbol{\omega}_i^* \\ -\Delta \boldsymbol{\omega}_i^* = \mathbf{curl} \mathbf{curl} \boldsymbol{\omega}_i^* = \mathbf{0} \\ \text{div} \boldsymbol{\omega}_i^* = 0, \quad \text{div} \boldsymbol{\psi}_i = 0 \\ (\boldsymbol{\omega}_i^0 + \boldsymbol{\omega}_i^*) \cdot \mathbf{n}|_{\Gamma_t} = \mathbf{0} \\ \boldsymbol{\psi}_i \times \mathbf{n}|_{\Gamma_t} = \mathbf{0}, \quad \mathbf{curl} \boldsymbol{\psi}_i \times \mathbf{n}|_{\Gamma_t} = \mathbf{0} \end{array} \right. \quad (31)$$

For each subsystem, a mixed formulation can be deduced by introducing the scalar fields λ_i^0, λ_i^* and η_i which permit respectively to weakly impose the divergence free properties of $\boldsymbol{\omega}_i^0, \boldsymbol{\omega}_i^*$ and $\boldsymbol{\psi}_i$ by acting as Lagrange multipliers. The systems $(S_{f,i})$ are then equivalent to the following weak form $(\Sigma_{f,i})$, given by (32) (see [19]).

$$(\Sigma_{f,i}) \left\{ \begin{array}{l} (\Sigma_{f,i}^{(1)}) \left\{ \begin{array}{l} \text{Find } (\boldsymbol{\omega}_i^0, \lambda_i^0) \in \mathbf{H}_0(\mathbf{curl}, \Omega_t) \times \mathbf{H}(\mathbf{grad}, \Omega_t) \text{ such that:} \\ \int_{\Omega_t} \mathbf{curl} \boldsymbol{\omega}_i^0 \cdot \mathbf{curl} \boldsymbol{\varphi}_i \, dx + \int_{\Omega_t} \mathbf{grad} \lambda_i^0 \cdot \boldsymbol{\varphi}_i \, dx = \\ \int_{\Omega_t} \mathbf{f}_i \cdot \mathbf{curl} \boldsymbol{\varphi}_i \, dx, \quad \forall \boldsymbol{\varphi}_i \in \mathbf{H}_0(\mathbf{curl}, \Omega_t) \\ \int_{\Omega_t} \boldsymbol{\omega}_i^0 \cdot \mathbf{grad} \mu_i \, dx = 0, \quad \forall \mu_i \in \mathbf{H}_0(\mathbf{grad}, \Omega_t) \end{array} \right. \\ (\Sigma_{f,i}^{(2)}) \left\{ \begin{array}{l} \text{Find } (\boldsymbol{\omega}_i^*, \lambda_i^*) \in \mathbf{H}(\mathbf{curl}, \Omega_t) \times \mathbf{H}(\mathbf{grad}, \Omega_t) \text{ and} \\ (\boldsymbol{\psi}_i, \eta_i) \in \mathbf{H}_0(\mathbf{curl}, \Omega_t) \times \mathbf{H}(\mathbf{grad}, \Omega_t) \text{ such that:} \\ \int_{\Omega_t} \boldsymbol{\omega}_i^* \cdot \boldsymbol{\varphi}_i \, dx - \int_{\Omega_t} \mathbf{curl} \boldsymbol{\psi}_i \cdot \mathbf{curl} \boldsymbol{\varphi}_i \, dx + \int_{\Omega_t} \mathbf{grad} \eta_i \cdot \boldsymbol{\varphi}_i \, dx = \\ - \int_{\Omega_t} \boldsymbol{\omega}_i^0 \cdot \boldsymbol{\varphi}_i \, dx, \quad \forall \boldsymbol{\varphi}_i \in \mathbf{H}(\mathbf{curl}, \Omega_t) \\ \int_{\Omega_t} \mathbf{curl} \boldsymbol{\omega}_i^* \cdot \mathbf{curl} \boldsymbol{\xi}_i \, dx + \int_{\Omega_t} \mathbf{grad} \lambda_i^* \cdot \boldsymbol{\xi}_i \, dx = 0, \quad \forall \boldsymbol{\xi}_i \in \mathbf{H}_0(\mathbf{curl}, \Omega_t) \\ \int_{\Omega_t} \boldsymbol{\psi}_i \cdot \mathbf{grad} \chi_i \, dx = 0, \quad \forall \chi_i \in \mathbf{H}_0(\mathbf{grad}, \Omega_t) \\ \int_{\Omega_t} (\boldsymbol{\omega}_i^0 + \boldsymbol{\omega}_i^*) \cdot \mathbf{grad} \mu_i \, dx = 0, \quad \forall \mu_i \in \mathbf{H}(\mathbf{grad}, \Omega_t) \end{array} \right. \end{array} \right. \quad (32)$$

It is important to mention that the condition $(\boldsymbol{\omega}_i^0 + \boldsymbol{\omega}_i^*) \cdot \mathbf{n} = 0$ on Γ_t is implicitly impose by choosing the test functions μ_i in $\mathbf{H}(\mathbf{grad}, \Omega_t)$; and for the boundary condition $\mathbf{curl} \boldsymbol{\psi}_i \times \mathbf{n} = 0$ on Γ_t , by choosing in $(\Sigma_{f,i}^{(2)})$ the test functions $\boldsymbol{\varphi}_i$ in $\mathbf{H}(\mathbf{curl}, \Omega_t)$ and not in $\mathbf{H}_0(\mathbf{curl}, \Omega_t)$.

By sequentially solve $(\Sigma_{m,i})$, then $(\Sigma_{f,i}^{(1)})$, and lastly $(\Sigma_{f,i}^{(2)})$ for $i = \{1, 2\}$, the desired velocities are finally obtained by $\mathbf{v}_1 = \mathbf{curl} \boldsymbol{\psi}_1$ and $\mathbf{v}_2 = \mathbf{curl} \boldsymbol{\psi}_2$. The practical implementation with high order basis functions and discrete form of the full system solved are detailed in Appendix. The plots of the calculated magnetic fields, the corresponding forces and the resulting velocities are provided by FIG. 4.

As expected, the magnetic fields created by the magnets remains concentrated in the area between each of them, and so does the electromagnetic forces. The velocity profiles are exactly those required, with one vortex created by

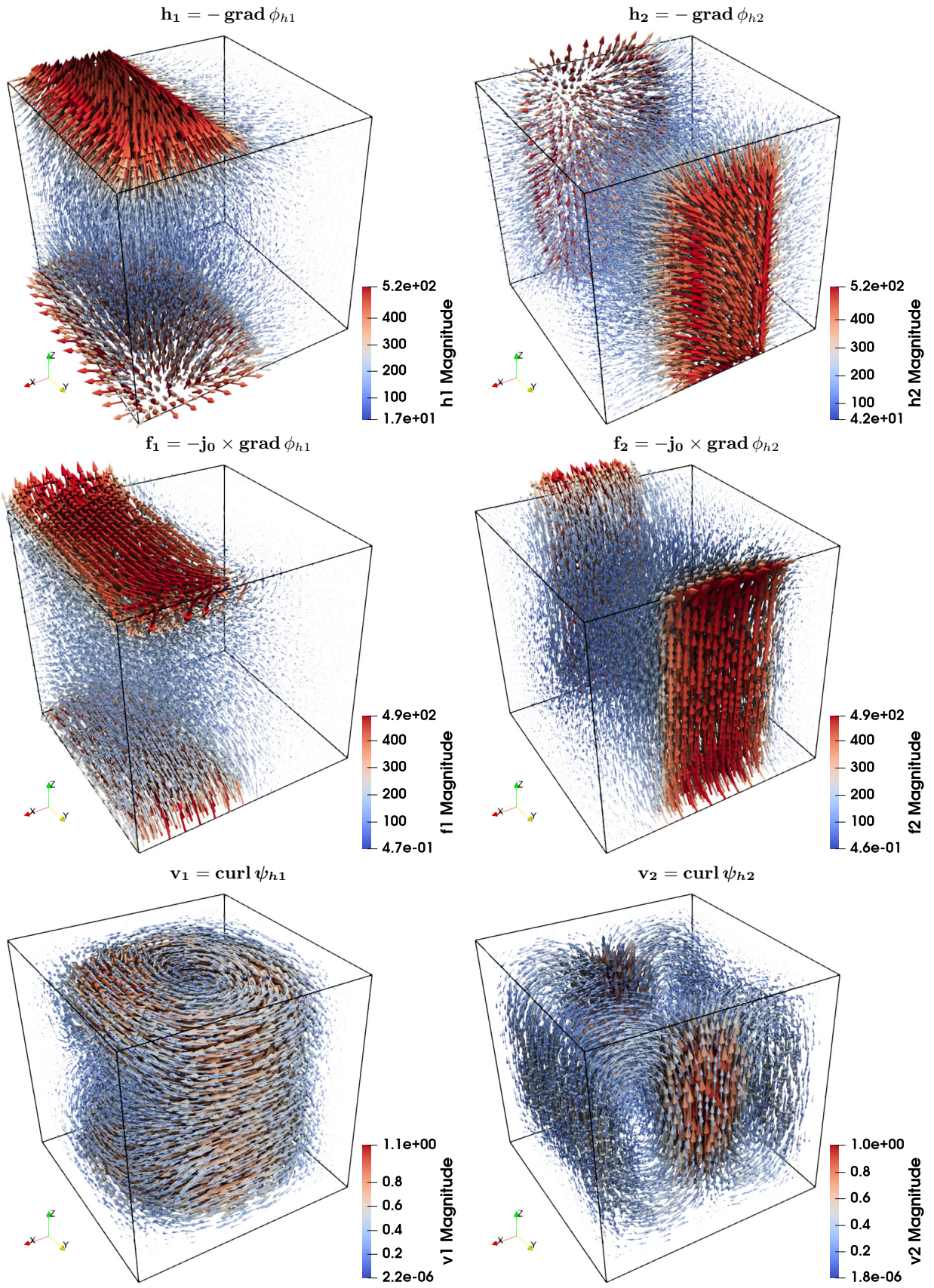


FIG. 4. Plots of calculated non-dimensionnal fields: \mathbf{h}_1 and \mathbf{h}_2 magnetic fields, corresponding forces \mathbf{f}_1 and \mathbf{f}_2 , and resulting \mathbf{v}_1 and \mathbf{v}_2 velocities.

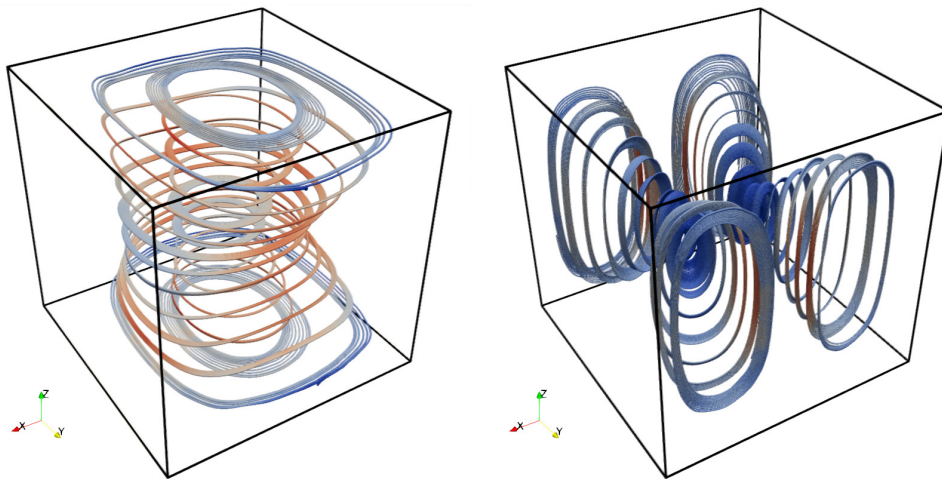


FIG. 5. Examples of velocities streamlines (\mathbf{v}_1 on left and \mathbf{v}_2 on right)

magnets #1 and two vortices created by magnets #2. To make this clearer, a few streamlines of \mathbf{v}_1 and \mathbf{v}_2 are also displayed in the FIG. 5.

At the end of the procedure, the two velocity fields are exported to a regular grid of $100 \times 100 \times 100$ points recovering the whole tank domain Ω_t . Of course, the values are computed thanks to our high order basis functions in order to keep the best possible accuracy. These export files constitute the final results of the numerical procedure described in this section, and are the starting point of the study of the chaotic behaviour detailed in the following.

IV. STUDY OF THE CHAOTIC BEHAVIOUR AND MIXING ANALYSIS

A. Highlighting and quantifying chaos

1. Trajectories and initial condition sensitivity

From now on, we will assume that it will always be possible to modulate the velocity fields \mathbf{v}_1 and \mathbf{v}_2 (by adjusting the magnet length, for example) and that the total velocity \mathbf{v} can be written as :

$$\mathbf{v} = \alpha \mathbf{v}_1 + (1 - \alpha) \mathbf{v}_2, \quad \text{for } \alpha \in [0, 1] \quad (33)$$

with α the convex combination coefficient of the two velocity fields. To find out the value of this velocity field at any point $\mathbf{x} = (x, y, z)$ in the tank, we simply interpolate by cubic spline interpolation the values calculated in the previous section. In the following, these interpolated functions will be still denoted \mathbf{v}_1 and \mathbf{v}_2 .

The key point of this part is to find out which α value gives the best possible mixing. To do this, we will study the nonlinear dynamic system corresponding to the trajectory followed by a fictitious particle (called tracer) initially located at \mathbf{x}_0 . In our case, this reads as:

$$\begin{cases} \frac{d\mathbf{x}}{dt} = \dot{\mathbf{x}}(t) = \alpha \mathbf{v}_1(\mathbf{x}(t)) + (1 - \alpha) \mathbf{v}_2(\mathbf{x}(t)) \\ \mathbf{x}(0) = \mathbf{x}_0 = (x_0, y_0, z_0) \end{cases} \quad (34)$$

Since the velocities are non-dimensional, the time involved in the equations will be expressed in non-dimensional units of time (u.t.).

The ordinary differential system (34) has been implemented with the Julia programming language using the DynamicalSystemsBase.jl package (and its subset ChaosTool.jl) [21]. We choose a solver based on an Adams-Bashforth explicit method: a fixed time step fifth order Adams-Bashforth-Moulton method, where a 5th order Adams-Bashforth method work as predictor and an Adams-Moulton 4-steps method for the corrector. Runge-Kutta method of order 4 is used to calculate starting values. Throughout the rest of this document, the time step is fixed to a value of $5 \cdot 10^{-4}$ u.t.

To get started, some trajectories are mapped out in order to study the sensibility to initials conditions. Three very close starting points are chosen: $\mathbf{x}_0 = (0.15, 0.15, 0.15)$, $\mathbf{x}_{01} = \mathbf{x}_0 + \varepsilon$ and $\mathbf{x}_{02} = \mathbf{x}_0 - \varepsilon$, with $\varepsilon = (1, 1, 1) \cdot 10^{-3}$. The

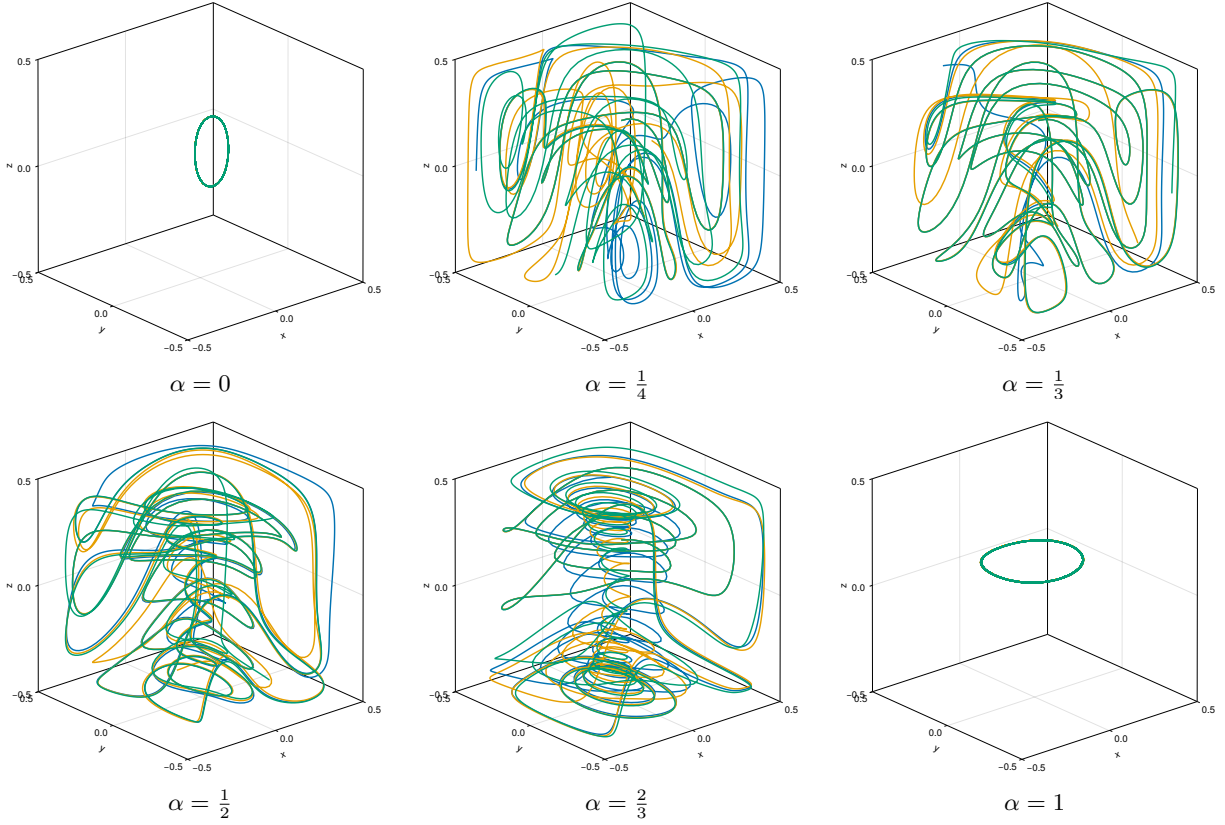


FIG. 6. Beginning of trajectories for several α values and for 3 starting points: $\mathbf{x}_0 = (0.15, 0.15, 0.15)$ (orange), $\mathbf{x}_{01} = \mathbf{x}_0 + \boldsymbol{\varepsilon}$ (blue) and $\mathbf{x}_{02} = \mathbf{x}_0 - \boldsymbol{\varepsilon}$ (green), with $\boldsymbol{\varepsilon} = (1, 1, 1) \cdot 10^{-3}$

beginnings of the three corresponding trajectories, for six α values arbitrary chosen between 0 and 1, are plotted in the FIG. 6.

First of all, we can see that the results of the previous section can be found in the cases $\alpha = 0$ ($\mathbf{v} = \mathbf{v}_2$) and $\alpha = 1$ ($\mathbf{v} = \mathbf{v}_1$). The trajectories have exactly the same regular shape as those shown in FIG. 5, and are merged for the three points from which they come from. For all other α values between these two extremes, trajectory shapes are much less regular (see FIG. 6). Stretching and good coverage of the tank space can clearly be observed. Moreover, they always end up deviating from each other, reflecting a sensitivity to initial conditions specific to chaotic behavior. This effect is particularly pronounced for $\alpha \simeq 0.25$, but always presents for other values of α .

It is therefore necessary to study deeper the impact of the α coefficient, using other tools such as Poincaré surfaces of sections and Lyapunov exponents.

2. Poincaré sections

For the single starting point $\mathbf{x}_0 = (0.15, 0.15, 0.15)$, and only for it, we draw the corresponding Poincaré sections in the $z = 0$ plane. They are represented for eight α values equally distributed between 0.2 and 0.6 on FIG. 7. It is important to point out that these plots have been obtained for a unique starting point, and not for a set of several points tightened around the initial condition. In the three cases $\alpha = 0.3, 0.4$ and 0.55 , just a second starting point very close to \mathbf{x}_0 has been added to obtain a similar number of impact points for all sections. The high densities of the plots show that the problem is solved with very good accuracy.

First, we can see in FIG. 7 that most of the Poincaré sections are covered, which means that the entire tank is explored by each trajectory. This is reassuring in terms of mixing efficiency. Nonetheless, we note the presence of holes in each case. This seems to indicate the presence of attractors, which must take the form of torii of periodic trajectories. Depending on the α coefficient, the position of these holes varies, with a $+$ -shaped placement for low α values and a \times -shape for higher values. The changeover seems to take place around $\alpha = 0.45$.

To better visualize these attractors, a 3D plot is shown in FIG. 8. For two α values (0.25 and 0.5), the beginning

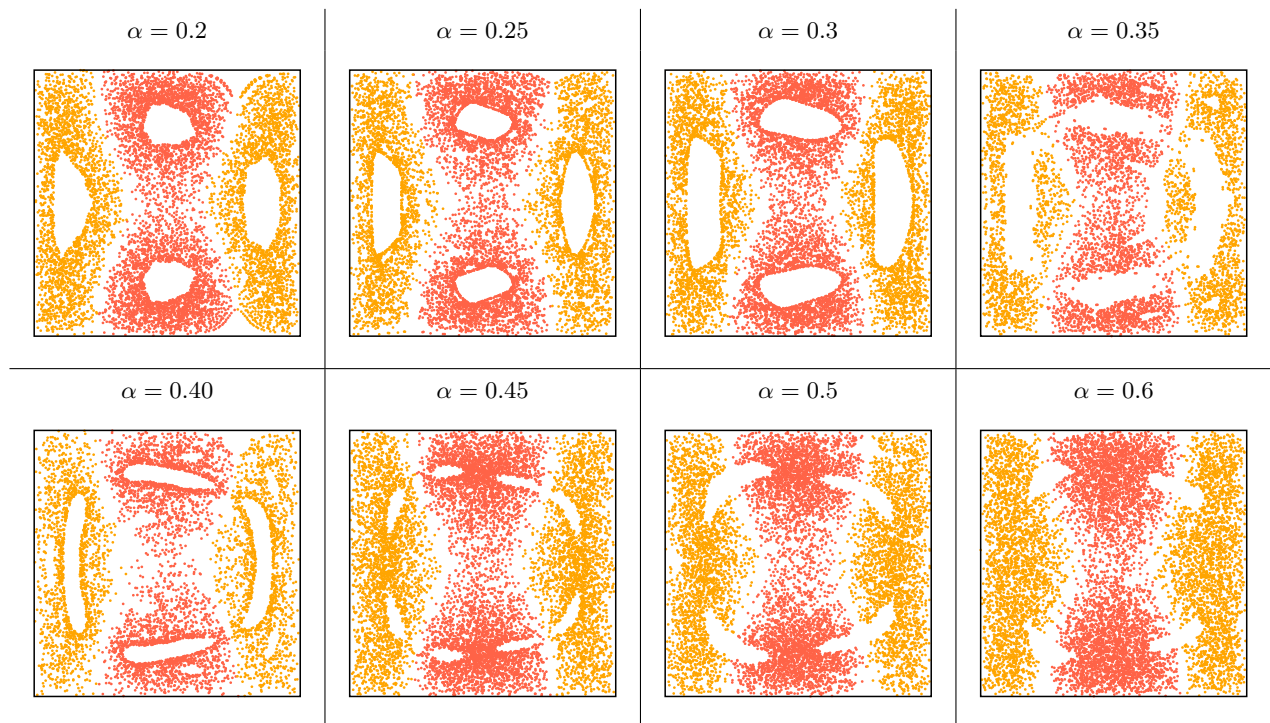


FIG. 7. Influence of α coefficient on the size and location of tori of periodic trajectories: dead zones represented by a hole in the Poincaré surfaces of sections ($z = 0$, $\mathbf{x}_0 = (0.15, 0.15, 0.15)$), the darker color corresponds to outgoing points and the lighter color to incoming points.

of trajectories are plotted for the previous starting point ($\mathbf{x}_0 = (0.15, 0.15, 0.15)$) and for points taken in one or two holes. The corresponding Poincaré sections $z = 0$ have been added alongside. The plots clearly show the attractors inside the orange chaotic trajectory. We can see one torus for the $\alpha = 0.25$ case, corresponding to the $+$ -shaped holes. For the $\alpha = 0.5$ case where the holes follow an \times -shape, two tori are present. However, even in the presence of these attractors, the flow studied may be chaotic from a global point of view. To characterize this, we will calculate some Lyapunov exponents in the next section.

Before that, and to conclude this paragraph, we can plot in FIG. 9 a set of Poincaré sections (in three planes in each direction of space), still for the same starting point and in the $\alpha = 0.45$ case, which seems to be the one where attractors are less prominent. Indeed, the plots clearly show that the entire space is almost visited by the particle, suggesting that mixing is efficient.

3. Lyapunov exponents computation

Lyapunov exponents are often used to quantify deterministic chaos. For a trajectory $\mathbf{x}(t)$ of a chaotic dynamical system, we perturb the initial position $\mathbf{x}(0) = \mathbf{x}_0$ at time $t = 0$ by \mathbf{y}_0 with $\delta_0 = \|\mathbf{x}_0 - \mathbf{y}_0\|$. As time t goes on, the perturbed trajectory \mathbf{y} moves further and further away from \mathbf{x} with a distance $\delta(t) \simeq \delta_0 \exp(\lambda t)$ where the real number λ , called Lyapunov exponent, is positive in the case of a chaotic system. Looking for perturbations along the three axes of the frame (O, x, y, z) , leads to three Lyapunov exponents λ_1, λ_2 and λ_3 . For the dynamical system (34), we consider a perturbation matrix Y according to the three cardinal axes which then satisfies the linearized dynamical system $\dot{Y}(t) = \nabla \mathbf{v}(\mathbf{x}(t)) Y(t)$ where \mathbf{v} is given by (33). The Lyapunov exponents can be computed from a QR -decomposition of the perturbation matrix $Y(t) = Q(t)R(t)$ with Q being an orthogonal matrix and R an upper triangular matrix with positive diagonal coefficients $R_{ii} > 0$ (see [22, Appendix A] and [23]):

$$\lambda_i = \lim_{t \rightarrow +\infty} \frac{1}{t} \ln R_{ii}(t), \quad \text{for } i = 1, 2, 3. \quad (35)$$

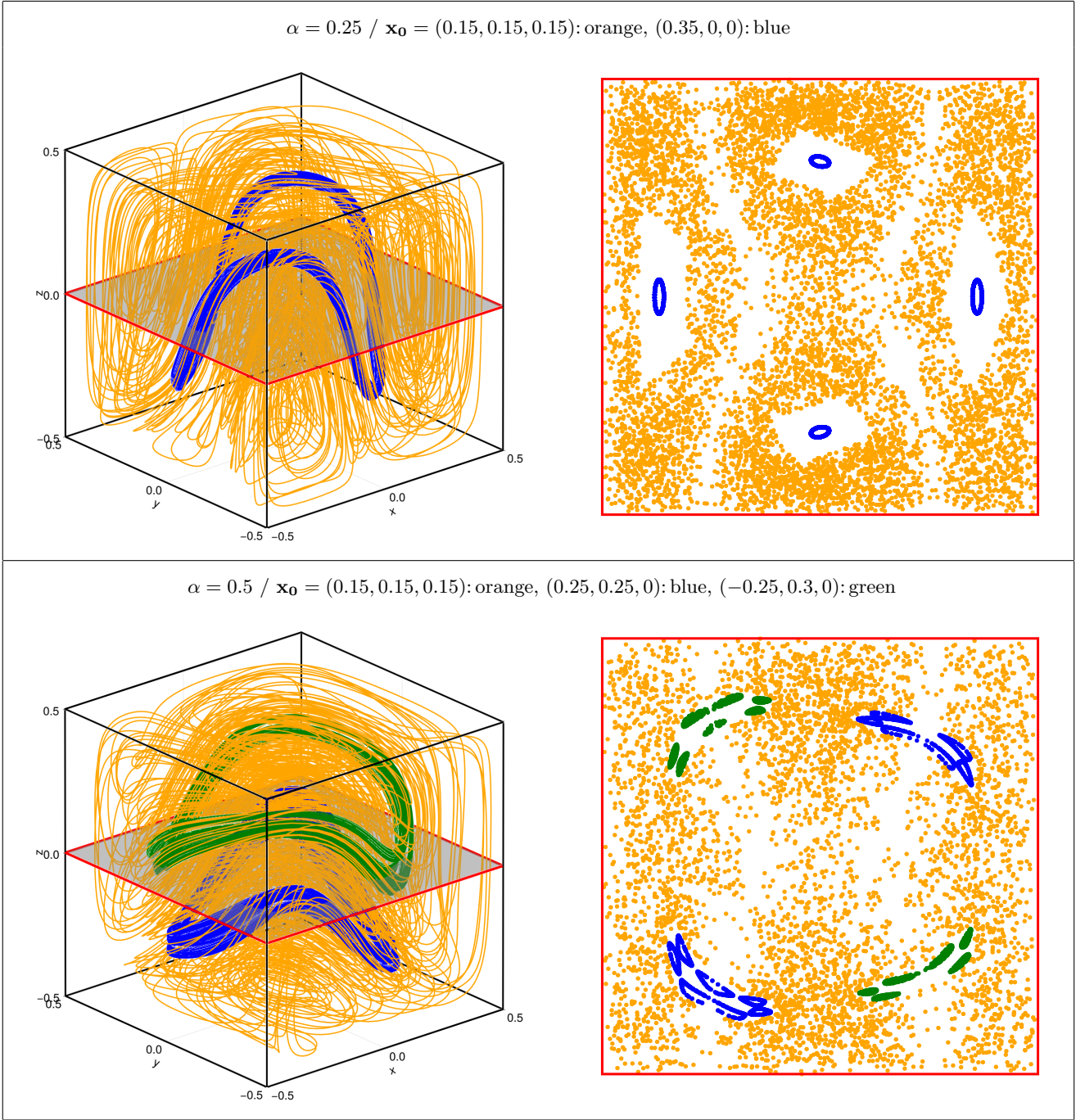


FIG. 8. Trajectories and corresponding $z = 0$ Poincaré surfaces of sections with highlight of one torus or two tori of periodic trajectories.

For practical numerical computations of the Lyapunov exponents, we perform iterated QR -decomposition of Y at discrete time t_k with time step Δt . We have $Y(t_k) = Q_k R_k$ with Y satisfying

$$\begin{cases} \dot{Y}(t) = \nabla \mathbf{v}(\mathbf{x}(t)) Y(t), & t \in [t_{k-1}, t_k] \\ Y(t_{k-1}) = Q_{k-1} \end{cases} \quad (36)$$

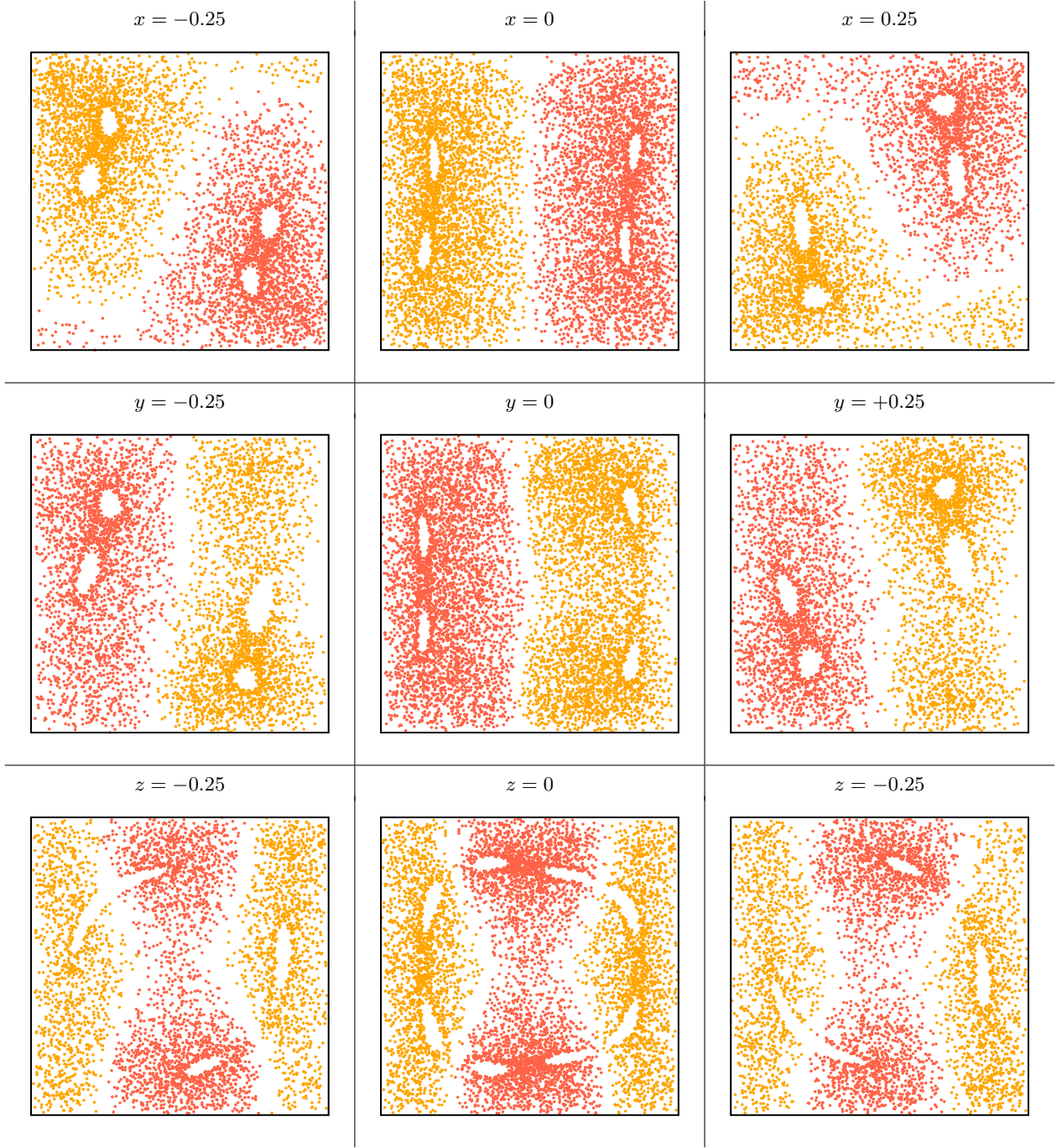


FIG. 9. Poincaré surfaces of sections for one single starting point $(0.15, 0.15, 0.15)$; the darker color corresponds to outgoing points and the lighter color to incoming points, $\alpha = 0.45$.

For a final time $T = N\Delta t$, we obtain the following iterated QR -decomposition with $Y(T) = Q_N R_N R_{N-1} \dots R_1$ and we compute the Lyapunov exponents according to the formula

$$\lambda_i \simeq \frac{1}{N\Delta t} \sum_{j=1}^N \ln (R_j)_{ii}. \quad (37)$$

The dynamical system (34) will present chaotic behavior if at least one Lyapunov exponent is positive. Since the velocity \mathbf{v} in (34) is divergence-free, the following property holds:

$$\lambda_1 + \lambda_2 + \lambda_3 = 0. \quad (38)$$

We emphasize that the Lyapunov exponents values depend on the initial position $\mathbf{x}(0) = \mathbf{x}_0$ of the trajectory. In a chaotic region (where the initial position \mathbf{x}_0 has been chosen), we necessarily get from (38)

$$\lambda_1 > 0, \lambda_2 = 0, \lambda_3 = -\lambda_1 < 0, \quad (39)$$

while in a smooth or regular region, we expect to have

$$\lambda_1 = \lambda_2 = \lambda_3 = 0. \quad (40)$$

This method can easily be called up using the Julia package mentioned previously [21]. We have modified the default implementation to preserve the history of terms calculated during the process. For our starting point $\mathbf{x}_0 = (0.15, 0.15, 0.15)$, and for the two α values of FIG. 8, we plot the Lyapunov coefficients λ_i versus the number of evolution steps N in FIG. 10.

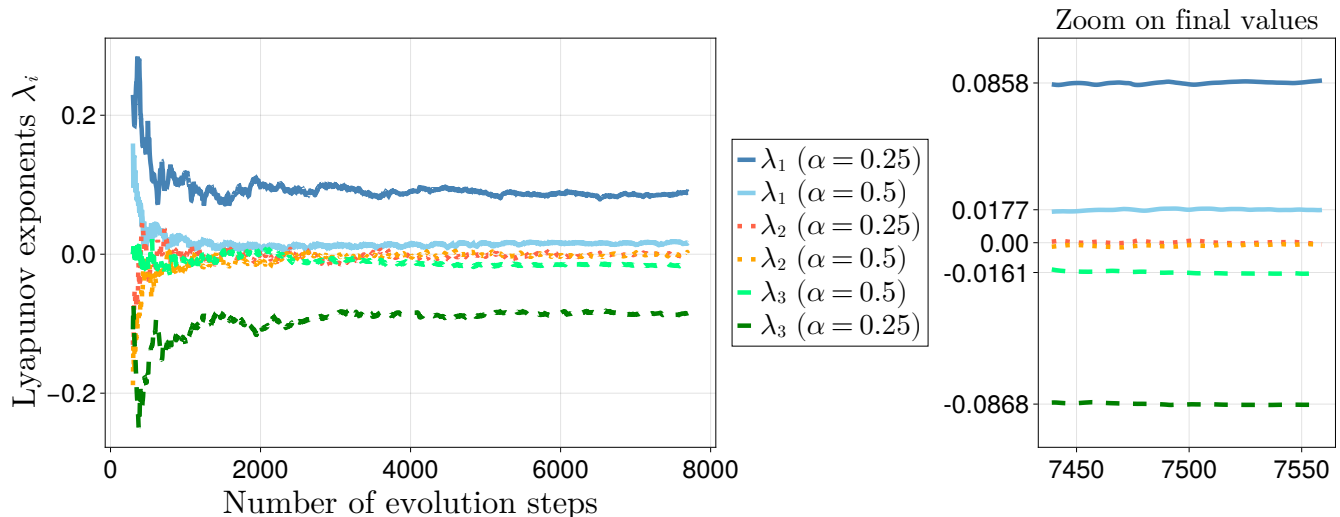


FIG. 10. Evolution of Lyapunov exponent values versus number of computation steps for the two previous cases ($\alpha = 0.25$ and 0.5 , $\mathbf{x}_0 = (0.15, 0.15, 0.15)$).

The shape of the curves corresponds well to relation (39), and the calculation converges fairly quickly, with a final value reach nearly 7,000 steps. This confirms our choice of ODE solver and associated time step. In both cases, we find a chaotic behavior with $\lambda_1 > 0$, but it is much more pronounced for $\alpha = 0.25$.

However, our main challenge now is to find a more "global" criterion that reflects the chaotic behavior of the entire flow. To do this, we calculate the average of the exponents associated with a set of 10×10 starting points distributed over a regular grid chosen in the half-plane $\{z = 0, x > 0\}$, for 100 values of alpha varying between 0 and 1. Results are displayed on FIG. 11.

Overall, the shapes of the curves appear to be coherent, with a pattern close to the expected case: $\lambda_1 > 0, \lambda_2 \simeq 0, \lambda_3 \simeq -\lambda_2$. The average of λ_1 is then always positive, except for the two extremes ($\alpha = 0$ or 1) where it is almost zero. Values between $\alpha = 0.1$ and 0.7 are sufficiently high to consider that the flow through the tank is chaotic and then, the mixing is efficient which confirms the results shown by Poincaré surfaces of sections.

Before closing this section, it is also interesting to observe the evolution of the maximal Lyapunov exponent λ_1 for starting points associated with the attractors seen previously. They are thus calculated as a function of alpha for the points $x_0 = (0.35, 0, 0)$ and $x_0 = (-0.25, 0.3, 0)$ corresponding respectively to the cases of one torus (in blue) and two tori (in green) of the FIG. 8. On the plot in FIG. 12, what had been observed is highlighted. The blue curve clearly shows a regular periodic trajectory for low α values and becomes chaotic as α increases. The green curve follows the opposite evolution, and the switch between the two behaviors occurs around $\alpha = 0.45$.

B. Mixing analysis

The Lyapunov exponents and Poincaré sections studied in the previous sections show that the dynamics of fluid points is chaotic. The system is therefore expected to mix efficiently. To quantify mixing, we divide the flow domain

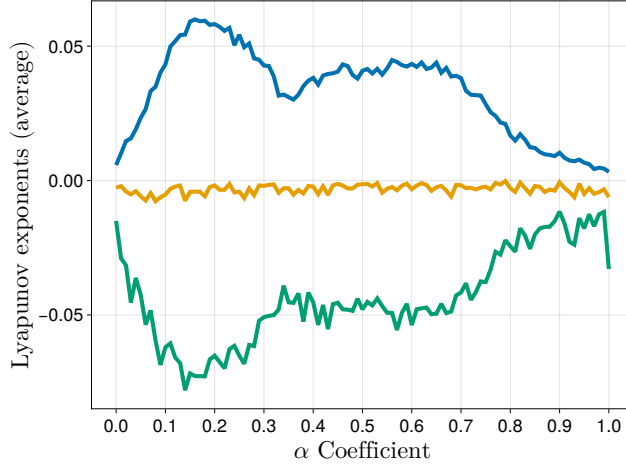


FIG. 11. Evolution of Lyapunov exponents versus α (averaged over 100 trajectories from a regular grid of starting points)

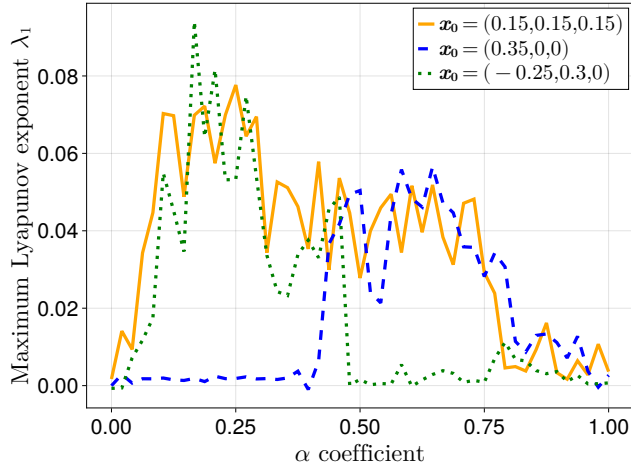


FIG. 12. Lyapunov exponents versus α for points of FIG. 8, the blue and green ones belongs to attractors: dash blue for one torus case and dot green otherwise.

into $N_c = 100^3$ cubic sub-domains ("cells"), then simulate the dispersion of clouds of N_p particles initially located within one of these cells near the center of the cube, by solving Eq. (34). We then derive two quantities of great interest for practical applications: the contamination rate and the final homogeneity. The former (denoted as $C(t)$ in the following) is the proportion of cells which were visited by some particles during the time interval $[0, t]$. The latter is based on the final particle density n_l , that is the number of particles in cell $l \in [1, N_c]$ at the final time of the simulation. At that time, we calculate the standard deviation σ of n_l , then the final homogeneity of the distribution defined as

$$H_\infty = 1 - \frac{\sigma}{\sigma_{\max}} \quad (41)$$

where σ_{\max} is the maximum value of the standard deviation (corresponding to the case where all particles gather in a single cell): $\sigma_{\max} = N_p \sqrt{N_c - 1} / N_c \simeq N_p / \sqrt{N_c}$. Poor mixing corresponds to $H_\infty = 0$, whereas efficient mixing corresponds to $H_\infty \simeq 1$.

The final time of the simulation of the cloud of particles is taken to be of a few convective times

$$t_c = \frac{a}{U} \quad (42)$$

where $U \simeq 0.1$ is an order of magnitude of the fluid velocity \mathbf{v} in the MHD computations. This corresponds to $t_c = 10$ non-dimensional units. Note that, as explained in the previous section, the contribution of each magnet has been

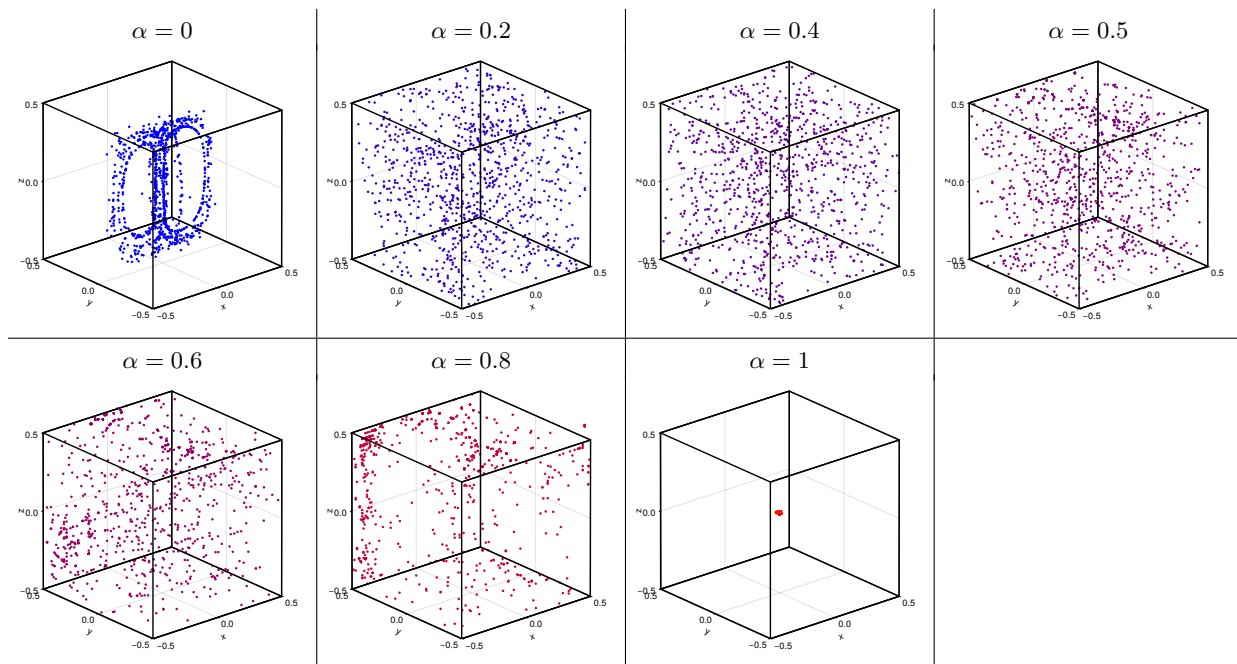


FIG. 13. Clouds of 1000 particles after 250 convective times, for various values of α . Particles were initially located in a $\frac{1}{100}$ sided cube at the center of the domain. The poloidal flow \mathbf{v}_2 ($\alpha = 0$) stretches the cloud but keeps it in a quasi-planar domain. The toroidal flow alone \mathbf{v}_1 ($\alpha = 1$) has very little effect on the tiny initial cloud.

parametrized by means of the parameter α (Eq. (33)): $\alpha = 1$ corresponds to stirring by the first magnet alone (blue colors in the following figures), whereas $\alpha = 0$ corresponds to the second magnet alone (red).

FIG. 13 shows a cloud of $N_p = 1000$ particles at $t = 250 t_c$, for various values of α . We observe that the shape of the cloud highly depends on α when α approaches 0 or 1, and mixing appears very poor there. Differences between transport by the poloidal flow (\mathbf{v}_2 alone, $\alpha = 0$) and the toroidal flow (\mathbf{v}_1 alone, $\alpha = 1$) are clearly visible. The poloidal flow alone highly deforms the cloud of particles within a quasi-planar domain. In contrast, the sole toroidal flow has little effect on the initial spot of particles, which rotates near the box center without being deformed.

FIG. 13 also suggests that there is a wide range of α 's where mixing seems efficient. This is confirmed in FIG. 14, as the contamination rate remains small for the extremal values of α (single magnet), whereas $C(t)$ increases quickly for intermediate values of α (two magnets).

Figure 14 shows the growth of contamination rates $C(t)$ for various α 's (upper left graph), as well as the final contamination rate C_∞ (upper right graph). For α in the range $[0.1, 0.6]$, mixing is efficient. It is slightly more efficient when $\alpha > 0.3$, though faster when $0.1 < \alpha < 0.3$. The largest contamination rate is above 90 %, and is obtained for $\alpha \simeq 0.5$.

The time of mixing is also an important parameter to quantify the quality of the device, and is sensitive to the parameter α . It is defined here as the time t_{mix} such that $C(t_{mix}) = 0.8$. The lower graph of Fig. 14 shows that mixing is faster for $0.1 < \alpha < 0.3$ than for α in the vicinity of 0.34. This fact can be correlated with the shape of the "global" Lyapunov exponent in FIG. 11. Indeed, we can see a dip in the value of λ_1 around this value of $\alpha = 0.34$. This demonstrates good agreement between our different means of estimating mixing efficiency.

The spatial quality of final mixing is quantified by means of the homogeneity coefficient H_∞ defined above. We observe that mixing is excellent for α between 0.1 and 0.45 (FIG. 15, left), and is a bit poorer when $\alpha > 0.6$, though it remains close to 80 % there.

Finally, choosing to use the product of final contamination C_∞ and final homogenization H_∞ as a criterion for mixing efficiency (as plotted on the right of FIG. 15), we can say that between $\alpha = 0.1$ and 0.6, mixing is very effective (greater than 80%).

V. CONCLUDING REMARKS

The proposed MHD device provides good overall mixing of a viscous fluid. The velocity fields it generates effectively produce a three-dimensional Stokes flow structure corresponding to a single vortex superposed with an orthogonal

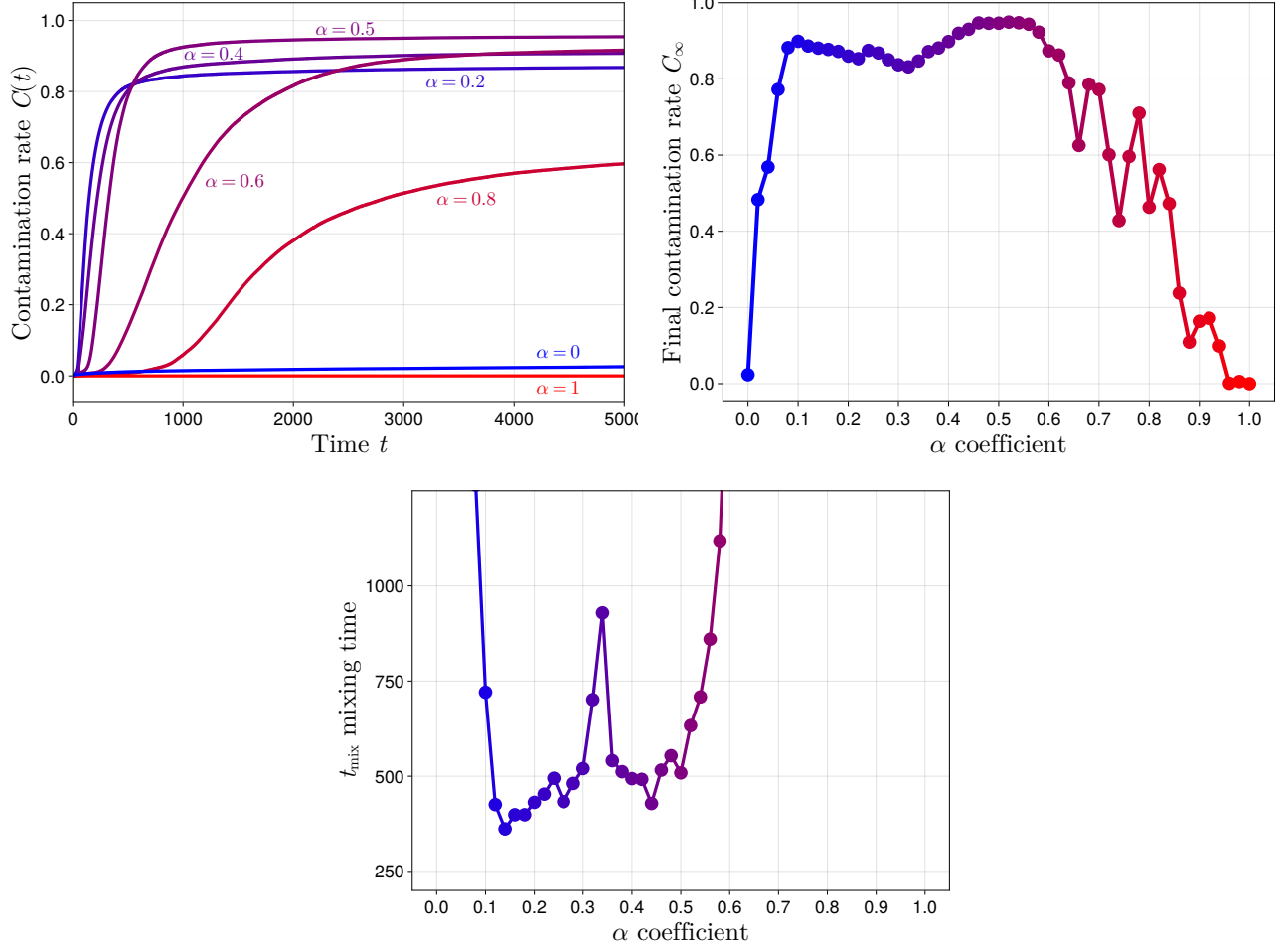


FIG. 14. Top graph left: contamination rate $C(t)$ versus time for various values of α from 0 (blue) to 1 (red). Top graph right: final values of C_∞ , at $t = 2500 = 250t_c$. Lower graph: time of mixing (defined by $C(t_{\text{mix}}) = 0.8$), versus α .

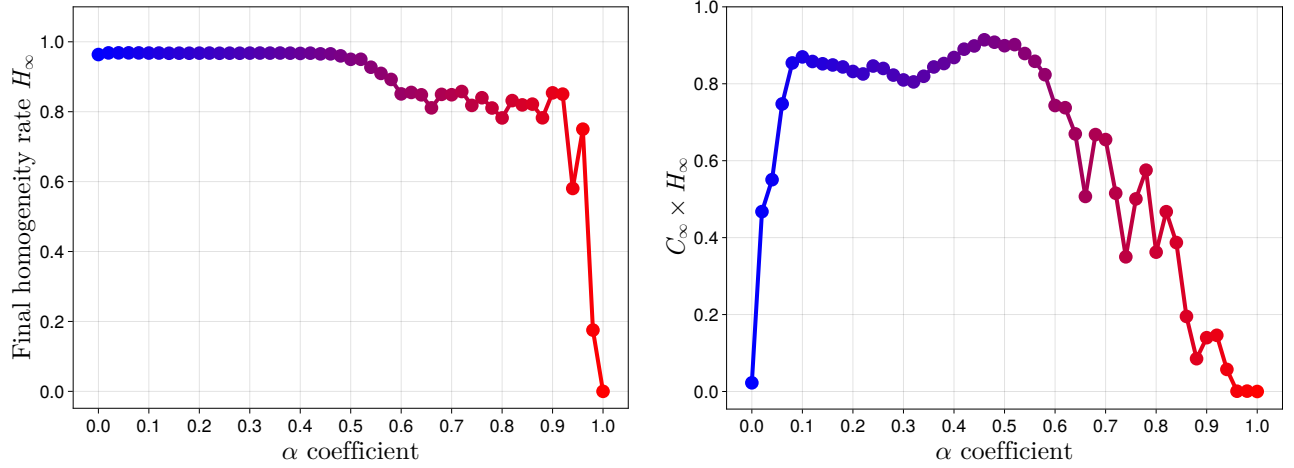


FIG. 15. Final homogeneity H_∞ versus α (left); product $C_\infty \times H_\infty$ versus α (right)

double vortex. A novel weak vorticity – stream-function formulation, based on the mixed finite element method has been specially developed and implemented to calculate these velocity fields. The accuracy of the results obtained is clearly demonstrated by the quality of the resulting plots. Thus, thanks to well-chosen Poincaré sections and multiple Lyapunov exponent computations, it has been shown that a combination of these two velocity fields produces particle trajectories in the fluid that are indeed chaotic. Calling α the coefficient of linear combination of the two velocity fields, it was shown that for a wide range of α values, mixing appears to be particularly efficient in terms of contamination and homogeneity rates. Following this theoretical study, the authors recommend using a value of α between 0.1 and 0.6, and more especially close to $\alpha = 0.45$ for best efficiency.

For the time being, the results obtained are based exclusively on simulations. In the near future, a demonstrator will be set up with the creation of an experimental bench. A real device will be design with the help of the present study, and then we will carry out tests to validate experimentally the results presented in this article.

Appendix: Implementation of numerical fields computation

In this part, we describe the main steps involved in the numerical resolution of the systems described in the previous one. The first step consists in generating the meshing of the studied geometry. For this purpose, the free and open-source software Gmsh is used [24]. The mesh size in the whole domain is controlled by the number n_e of elements on the edges of the cubic tank. We therefore impose a structured mesh in Ω_t ; and outside, the characteristic length of the elements is then gradually scaled up as the distance from the tank increases, until the boundary Γ_∞ is reached. The mesh of the domain with the chosen control parameter value ($n_e = 15$) is displayed on FIG. 3, and some characteristics are provided in TABLE I.

TABLE I. Some statistics of the chosen mesh

Domain	Nodes	Triangles	Tetrahedra
Ω	18,350	6,866	107,674
Ω_t	3,423	3,256	15,964

Afterwards, the formulations detailed in section III were then implemented in C++ code using the free and open-source GmshFEM library [25, 26]. Thanks to this library, it is relatively easy to define the approximate subspaces based on our mesh of the global needed function spaces $H_0(\mathbf{grad}, \Omega)$, $H(\mathbf{grad}, \Omega_t)$, $H_0(\mathbf{grad}, \Omega_t)$, $\mathbf{H}(\mathbf{curl}, \Omega_t)$, and $\mathbf{H}_0(\mathbf{curl}, \Omega_t)$. These finite dimensional function spaces are respectively called $W_0^0(\Omega)$, $W^0(\Omega_t)$, $W_0^0(\Omega_t)$, $W^1(\Omega_t)$ and $W_0^1(\Omega_t)$, and are defined thanks to hierarchical basis functions. The three first spaces are generated using 0-form nodal basis functions which are the classical nodal basis functions of Lagrange elements, their order are noted p_n . The two other spaces $W^1(\Omega_t)$ and $W_0^1(\Omega_t)$ are generated by 1-form edge basis functions of order p_e built with the same functions as the previous ones, see [14, 15, 27] for details.

The numerical implementation and runs were performed on a dedicated workstation with 48 threads @3.5 GHz and 192 GiB of RAM. For the best possible accuracy of results, we choose to use high order elements with an interpolation order of $p_n = 4$ for the nodal basis functions of $W_0^0(\Omega)$, $W^0(\Omega_t)$ and $W_0^0(\Omega_t)$, and $p_e = 3$ for the edge basis functions of $W^1(\Omega_t)$ and $W_0^1(\Omega_t)$. These values combined with a mesh parameterized with the chosen value of n_e allow us to make the best use of all our computing resources. The synthesis of the systems we solve (using the MUMPS direct solver [28]) is given by (A.1), and some details upon the numerical runs are reported in TABLE II.

TABLE II. Details of the numerical resolution ($n_e = 15$, $p_n = 4$, $p_e = 3$)

System	$(\Sigma_{hm,i})$	$(\Sigma_{hf,i}^{(1)})$	$(\Sigma_{hf,i}^{(2)})$
DOFs	1,207,089	527,823	1,198,914
Assembling time	2.47 sec	1.92 sec	4.12 sec
Solving time	208 sec	92 sec	3050 sec

The very low value of assembling time highlights the efficiency of the chosen solver. Moreover, even if the computation time of the last system $(\Sigma_{hf,i}^{(2)})$ seems high compared to the others (due to a non-symmetry of the stiffness matrix), the duration of the whole resolution remains largely acceptable for such a quite big problem.

- magnetohydrodynamic quadripolar flow, *Phys. Rev. E* **63**, 056309 (2001).
- [12] This assumption had been verified by *a posteriori* simulations showing that the L_2 norm over the tank domain of the relative difference on forces, between with and without neglecting the current density contribution, is less than 0.1% (with typical range of values of source terms).
- [13] J. C. Nédélec, Mixed finite elements in \mathbb{R}^3 , *Numer Math (Heidelb)* **35**, 315 (1980).
- [14] Z. Ren and N. Ida, High order differential form-based elements for the computation of electromagnetic field, *IEEE Trans. Magn.* **36**, 1472 (2000).
- [15] C. Geuzaine, *High order hybrid finite element schemes for Maxwell's equations taking thin structures and global quantities into account*, Ph.D. thesis, ULiège - Université de Liège (2001).
- [16] J. C. Nédélec, A new family of mixed finite elements in \mathbb{R}^3 , *Numer Math (Heidelb)* **50**, 57 (1986).
- [17] J. F. Imhoff, G. Meunier, X. Brunotte, and J. C. Sabonnadière, An original solution for unbounded electromagnetic 2D- and 3D-problems throughout the finite element method, *IEEE Trans. Magn.* **26**, 1659 (1990).
- [18] C. Amrouche, C. Bernardi, M. Dauge, and V. Girault, Vector potentials in three-dimensional non-smooth domains, *Math. Methods Appl. Sci.* **21**, 823 (1998).
- [19] M. Amara, H. Barucq, and M. Duloué, Une formulation mixte convergente pour le système de stokes tridimensionnel, *C. R. Acad. Sci. - Series I - Mathematics* **328**, 935 (1999).
- [20] M. Amara and C. Bernardi, Convergence of a finite element discretization of the navier-stokes equations in vorticity and stream function formulation, *Esaim Math Model Numer Anal* **33**, 1033 (1999).
- [21] G. Datseris, *DynamicalSystems.jl: a Julia software library for chaos and nonlinear dynamics*, *JOSS* **3**, 598 (2018).
- [22] G. Datseris and U. Parlitz, *Nonlinear dynamics: A concise introduction interlaced with code* (Springer Nature, Cham, Switzerland, 2022).
- [23] J. P. Eckmann and D. Ruelle, Ergodic theory of chaos and strange attractors, *Rev. Mod. Phys.* **57**, 617 (1985).
- [24] C. Geuzaine and J.-F. Remacle, Gmsh: A 3-D finite element mesh generator with built-in pre- and post-processing facilities, *Int J Numer Methods Eng* **79**, 1309 (2009).
- [25] A. Royer, E. Béchet, and C. Geuzaine, Gmsh-Fem: An efficient finite element library based on Gmsh, in *14th World Congress on Computational Mechanics (WCCM), ECCOMAS Congress 2020* (2021) pp. 1–13.
- [26] A. Royer, *Efficient finite element methods for solving high-frequency time-harmonic acoustic wave problems in heterogeneous media*, Ph.D. thesis, ULiège - Université de Liège [Faculté des Sciences Appliquées], Belgique, Belgium (2023).
- [27] P. Solin, K. Segeth, and I. Dolezel, *Higher-Order Finite Element Methods*, 1st ed., edited by Chapman and Hall (CRC, 2003).
- [28] P. Amestoy, A. Buttari, J.-Y. L'Excellent, and T. Mary, Performance and Scalability of the Block Low-Rank Multifrontal Factorization on Multicore Architectures, *ACM Trans Math Softw* **45**, 2:1 (2019).